



Thermal Conductivity Switching in Pd-Catalyzed Gd and GdH₂ Films Upon Gasochromic Hydrogenation and Dehydrogenation

Riko Hirata¹ · Yuichiro Yamashita^{1,2} · Takashi Yagi^{1,2} · Makoto Kashiwagi¹ · Satoshi Takeya² · Yuki Oguchi³ · Fabio Iesari⁴ · Toshihiro Okajima^{1,4} · Naoyuki Taketoshi^{1,2} · Yuzo Shigesato¹

Received: 8 December 2023 / Accepted: 21 December 2023 / Published online: 21 February 2024
© The Author(s) 2024

Abstract

Thermal conductivity switching in Pd-catalyzed Gd hydride films was investigated using in situ analyses of electrical, optical, structural, and thermophysical properties upon gasochromic hydrogenation/dehydrogenation at room temperature. These reactions allow the films to reversibly switch between the metallic (GdH₂) phase in the hydrogenated state and the semiconductor (GdH₃) phase in the dehydrogenated state. We fabricated three-layered films comprising Pd (5 nm)/Gd or GdH₂ (300 nm)/Mo (100 nm) using DC magnetron sputtering using Pd, Gd, and Mo targets, respectively, on unheated synthetic quartz substrates. Ar or mixture of Ar + H₂ (H₂: 5 % to 50 %) gases were used for the deposition of the Gd or GdH₂ films, respectively. The thermal conductivities of the Gd or GdH₂ films were analyzed using in situ rear-heating/rear-detection type time-domain picosecond pulsed light heating thermoreflectance measurements by employing a gas mixture of N₂/Ar and H₂ (H₂: 3 %) at 1 atm, which is below the explosive limit for hydrogen. The thermal conductivities of Gd and GdH₂ films were measured for one and two hydro-/dehydrogenation cycles, respectively. The thermal switching ratios of the ON state thermal conductivity to the OFF state thermal conductivity were 6.4 and 2.9–5.4 for the Gd film and the GdH₂ (H₂: 5 %–50 %) films, respectively. The thermal conductivity of the Gd hydrides films changed along with those estimated from the Wiedemann–Franz Law and electrical conductivities.

Keywords Gadolinium · Gadolinium hydrides · Gasochromic hydrogenation/dehydrogenation · In situ time-domain thermoreflectance · Switchable mirror materials · Thermal conductivity switching

1 Introduction

The reuse of waste heat is one of the emerging social issues to improve energy efficiency. Technologies that provide heat flow control such as thermal diodes, transistors, regulators, and switches have attracted remarkable interest in thermal engineering recently [1]. Thermal conductivity switching realizes heat flow control owing to a sharp contrast in thermal conductivities between ON/OFF states. The ON/OFF states of thermal conductivity have been controlled using changes in structures [2, 3], phase transitions [4, 5], and chemical reactions [6–9] obtained upon various external fields such as UV irradiations [9], application of voltages, and magnetic fields.

Recently, a high contrast in thermal conductivity change has been reported for a switchable mirror material [10, 11]. The switchable mirror is used for the control of optical properties between the semiconductor state (transparent) and the metal state (opaque) obtained via hydro-/dehydrogenation, respectively [12–14]. The thermal conductivity changes of a Pd-catalyzed Ni–Mg thin film, one of the switchable mirror materials controlled using the reaction of dilute H₂ gas, reached a factor of 14 between the ON/OFF states [10]. In the metal state, the thermal conductivity is mainly due to the contribution of free electrons. In contrast, phonons dominate the thermal conductivity in the semiconductor state, resulting in a low thermal conductivity.

Although switchable mirror materials are expected to exhibit excellent performance in thermal conductivity switching, a large volume change associated with hydro-/dehydrogenation hinders durability. Approximately 25 % of volume expansion was observed between Ni–Mg films and their hydrides [15]. Such a large volume change can cause cracks or the peeling of the film, decreasing the switching durability. The durability of switchable mirror materials must be improved by reducing volume expansion due to hydro-/dehydrogenation.

Gadolinium (Gd) is a switchable mirror material that can switch between a metallic dihydride (GdH₂) and a semiconducting trihydride (GdH₃). The linear volume expansion from GdH₂ to GdH₃ is approximately 3 %, which is smaller than that from Gd to its hydrides. The formation enthalpies from Gd to GdH₂ and from GdH₂ to GdH₃ are -197 kJ mol^{-1} and -50 kJ mol^{-1} [16], respectively. The reaction between GdH₂ and GdH₃ becomes reversible with the Pd catalyst [17]. The electrical conductivity of GdH₂ was reported to be $2.3 \times 10^6 \text{ S m}^{-1}$ [18], which is comparable to those of Ti ($2.33 \times 10^6 \text{ S m}^{-1}$ [19]) and Zr ($2.29 \times 10^6 \text{ S m}^{-1}$ [20]). Owing to the contribution of free electrons, the thermal conductivities of Ti and Zr are $21.9 \text{ W m}^{-1} \text{ K}^{-1}$ [21] and $19.7 \text{ W m}^{-1} \text{ K}^{-1}$ [22], respectively. Based on the Wiedemann–Franz law (WFL), metallic GdH₂ is expected to possess a relatively high thermal conductivity.

In this study, both Gd and GdH₂ films were synthesized via reactive direct current (DC) magnetron sputtering with various H₂ gas flow ratios. The prepared Pd-catalyzed Gd or GdH₂ films can be controlled via hydro-/dehydrogenation upon exposure to a dilute H₂ gas (3 %) and air at room temperature (RT), respectively. The performance of the thermal conductivity switching of the GdH₂ films was studied compared to that of the Gd film.

2 Experiments

2.1 Sample Preparation

For thermal conductivity measurements, we fabricated trilayer Pd/Gd/Mo or Pd/GdH₂/Mo films on an unheated synthetic quartz glass substrates, where a 100-nm-thick Mo underlayer acts as a transducer film for thermoreflectance measurements. The Mo layers were deposited via DC magnetron sputtering using a Mo target (99.95 % in purity, 3 inch in diameter), and 1.0 Pa of Ar was used as a sputtering gas with an applied DC power of 50 W. Gd or GdH₂ films with a nominal thickness of 300 nm were deposited on the Mo layers via reactive DC magnetron sputtering using a Gd target (99.99 % in purity, 3 inch in a diameter) with an applied DC power of 50 W. Target-substrate distance was fixed at 55 mm. For the deposition of Gd or GdH₂ films, 100 % Ar or mixture of Ar + H₂ (H₂: 5 %, 20 %, 30 %, and 50 %) gases were used, respectively, as the sputtering gases. The total gas flow during all the depositions was fixed at 10 sccm, where the Ar/H₂ ratios were controlled by their gas flow ratios. The back pressure was less than 4.0×10^{-4} Pa, and the total gas pressure during the deposition was kept at 1.0 Pa. Without exposure to the air, the surfaces of the Gd or GdH₂ films were covered with a 5-nm-thick Pd layer, which acts as a catalyst for gasochromic hydro-/dehydrogenation and protects the Gd or GdH₂ layers from oxidation. The Pd layers were deposited via DC sputtering using a sputtering gas of Ar (99.999 % in purity) at a total gas pressure of 0.5 Pa and a sputtering power of 10 W. The thickness of the Pd film was optimized for enhanced hydro-/dehydrogenation efficiency. All layers were synthesized without heating the substrate. We also fabricated bilayer Pd/Gd or Pd/GdH₂ films on synthetic quartz glass substrates for in situ X-ray diffraction (XRD), X-ray absorption fine structure (XAFS), optical transmittance, and electrical conductivity analyses. The deposition conditions for the Gd or GdH₂, Pd, and Mo films are listed in Table 1. Hereafter, the samples with the Gd film and the GdH₂ film in the as-deposited state were named “ad-Gd sample” and “ad-GdH₂ (H₂: 5 %) sample”, “ad-GdH₂ (H₂: 20 %) sample”,

Table 1 Deposition conditions for the Gd or all the GdH₂, Pd, and Mo films

	Gd or GdH ₂	Pd	Mo
Deposition method	dc magnetron sputtering		
Target	Gd (99.99 %)	Pd (99.99 %)	Mo (99.95 %)
Sputtering gas	Ar	Ar	Ar
Reactive gas	H ₂	–	–
H ₂ flow ratios, %	0, 5, 20, 30, 50	–	–
Total gas pressure, Pa	1.0	0.5	1.0
Back pressure, Pa	$< 4.0 \times 10^{-4}$		
Nominal thickness, nm	300	5	100
Substrate temperature	Room temperature		
DC power, W	50	10	50

“ad-GdH₂ (H₂: 30 %) sample”, and “ad-GdH₂ (H₂: 50 %) sample” for their H₂ flow ratios, respectively.

2.2 Optical Properties

In situ optical transmittance measurements were performed in the spectral range of 185–3300 nm using a spectrophotometer (UV-3600iPlus, Shimadzu) and the hydrogen-content-controlled vacuum chamber for the ad-Gd and ad-GdH₂ (H₂: 50 %) samples at RT and 1 atm. First, the transmittance spectra in the as-deposited state were measured under atmospheric conditions. The transmittance spectra in the hydrogenated state were measured after the chamber was replaced with a mixture of Ar and H₂ (3 %) gases. The transmittance spectra in the dehydrogenated state were measured after the chamber was replaced with the atmosphere.

2.3 Structural Analyses

The crystal structures of the Gd and Gd hydrides films in the hydro-/dehydrogenated states were analyzed at RT using in situ XRD. XRD measurements were conducted using Cu K_α radiation (Ultima III, Rigaku). First, the XRD patterns of the as-deposited state were measured under atmospheric conditions. The XRD patterns of the hydrogenated state were measured after the chamber was evacuated and replaced with a mixture of Ar and H₂ (3 %) gases (below the explosive limit for hydrogen) for the ad-Gd sample or a mixture of N₂ and H₂ (3 %) gases for the ad-GdH₂ (H₂: 50 %) sample for 2 h. The measurement in the dehydrogenated state was performed after the chamber was again evacuated and replaced with the air for 12 h. For the ad-GdH₂ (H₂: 5 %, 20 %, and 30 %) samples, XRD patterns of as-deposited and dehydrogenated states in the air were measured using XRD-6000 (Shimadzu).

The Gd L₃-edge XAFS spectra of the ad-Gd and ad-GdH₂ (H₂: 50 %) samples in the hydro-/dehydrogenated states were measured at beamlines BL5S2 and BL11S2 of AichiSR. Samples were placed inside a quartz flow cell, which allows for measurements under various gases. All XAFS measurements were performed in the fluorescence mode at RT and 1 atm.

Cross-sectional Transmission Electron Microscopy (TEM) observations were conducted on the as-deposited and dehydrogenated states of the ad-Gd and ad-GdH₂ (H₂: 50 %) samples using JEM-2100 (200 kV, JEOL).

2.4 Electrical Conductivity

The electrical conductivities of the ad-Gd and all the ad-GdH₂ samples in the as-deposited, hydrogenated, and dehydrogenated states were evaluated using the in situ four-point probe method (HL5500PC, ACCENT) with a parallel circuit model comprising Pd and Gd (or Gd hydrides) layers. The sheet resistances were measured on two-layer Pd/Gd or Pd/Gd hydrides samples at RT. The electrical conductivities of the Gd or Gd hydrides layers were calculated, where the sheet resistance of Pd was measured for a Pd monolayer film deposited on an unheated quartz glass substrate

under the same conditions listed in Table 1. The sheet resistance in the hydrogenated state was measured after the chamber was evacuated and replaced with the mixture of N_2 and H_2 (3 %) gases of 1 atm at RT, and that in the dehydrogenated state was measured after the chamber was replaced with the air of 1 atm at RT. The sheet resistances in each states were recorded when they reached at constant values.

2.5 Thermal Conductivity

The thermal conductivities of the Gd or Gd hydrides films were investigated using an in situ rear-heating/rear-detection type time-domain picosecond pulsed light heating thermoreflectance (TDTR) measurement apparatus [23], as shown in Fig. 1. The wavelength, pulse width, and power of the pump laser were 1550 nm, <0.5 ps, and 20 mW, respectively. The wavelength and pulse width, and power of the probe laser were 775 nm, <0.5 ps, and 1 mW, respectively. The reflected probe laser beam was

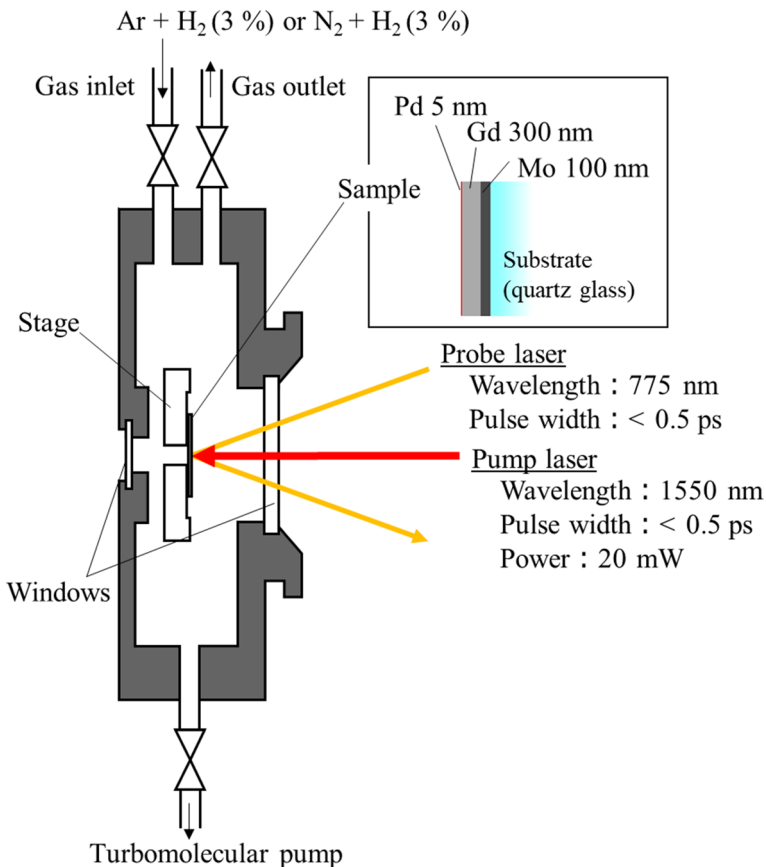


Fig. 1 Schematic diagram of an in situ rear-heating/rear-detection type time-domain thermoreflectance apparatus

measured using a Si photodiode and a lock-in amplifier. The lock-in phase signal was recorded against the delay time between pump and probe pulses. The sample temperatures upon pump laser heating were estimated as 315 K for the ad-Gd and ad-GdH₂ (H₂: 20, 30 %) samples, and 317 K for the ad-GdH₂ (H₂: 5, 50 %) samples.

First, the thermal conductivity in the as-deposited state was measured under atmospheric conditions. The thermal conductivity in the hydrogenated state was measured after the chamber was evacuated and replaced with a mixture of Ar (for the ad-Gd sample) or N₂ (for all the ad-GdH₂ samples) and H₂ (3 %) gases at 1 atm for 1 h. The thermal conductivity in the dehydrogenated state was measured after evacuating the chamber again and replacing the gas in the chamber with the air for 1 h. The same sequences were repeated for the second hydro-/dehydrogenated states for the ad-GdH₂ (H₂: 5 % and 50 %) samples. For the ad-GdH₂ (H₂: 20 % and 30 %) samples, the measurements in the second dehydrogenated state were carried out after the samples reached stable state. The thermal diffusivity and volumetric heat capacity for the Gd and Gd hydrides, and Gd/Mo and Gd hydrides/Mo boundary thermal resistances were evaluated based on the simulation of the phase signal, which solves the heat transport equation under the assumptions of unsteady one-dimensional heat conduction and bilateral semi-infinite substrates. As common fixed fitting parameters, the thermal diffusivity, volumetric heat capacity, and optical absorption coefficient at a wavelength of 1550 nm of the Mo film were $2.1 \times 10^{-5} \text{ m}^2 \text{ s}^{-1}$, $2.6 \times 10^6 \text{ J m}^{-3} \text{ K}^{-1}$, and $4.6 \times 10^7 \text{ m}^{-1}$, respectively. The thermophysical properties of the Pd layer were assumed to be same as those of the bulk: the thermal diffusivity, volumetric heat capacity, and film thickness were set to $2.5 \times 10^{-5} \text{ m}^2 \text{ s}^{-1}$ [24], $2.9 \times 10^6 \text{ J m}^{-3} \text{ K}^{-1}$, and 5 nm, respectively. The thermal effusivities of the quartz glass substrate were set to $1487 \text{ J m}^{-2} \text{ s}^{-0.5} \text{ K}^{-1}$ (for the ad-Gd and ad-GdH₂ (H₂: 20 % and 30 %) samples) and $1488 \text{ J m}^{-2} \text{ s}^{-0.5} \text{ K}^{-1}$ (for the ad-GdH₂ (H₂: 5 % and 50 %) samples), respectively. The volumetric heat capacity of Mo and Pd was calculated from the density and specific heat capacity shown in Ref. 24, and thermal diffusivity of Pd was calculated from the density, specific heat capacity and thermal conductivity shown in Ref. 24. The thermal effusivity of quartz glass substrate was also calculated from the thermal conductivity, specific heat capacity, and density shown in Ref. 24. The thicknesses of the ad-Gd and ad-GdH₂ (H₂: 50 %) samples in the as-deposited state were 300 nm and 301 nm, respectively, measured by a step-height meter. Considering the volume expansion, the thicknesses of the ad-Gd sample in the hydro-/dehydrogenated states were estimated as 322 nm and 313 nm, whereas those of the ad-GdH₂ (H₂: 50 %) sample in the hydro-/dehydrogenated states were 311 nm and 301 nm, respectively. The properties and thickness of the Mo layer were estimated in advance from Mo monolayer film measurements. All fitting parameters and determined properties are shown in Tables S1–S3 of Supplementary information.

3 Results and Discussions

3.1 Dynamic Structural Changes and Control of Hydro-/dehydrogenation

Figure 2 shows the results of the in situ XRD measurements on the as-deposited, hydrogenated, and dehydrogenated states of the ad-Gd and ad-GdH₂ (H₂: 50 %)

samples. The XRD patterns in the as-deposited and dehydrogenated states for ad-GdH₂ (H₂: 5 %, 20 %, and 30 %) samples are shown in Fig. S1 of Supplementary information. Figure 2(a) shows the XRD of the as-deposited state of the ad-Gd sample, where hexagonal close-packed structure and face-centered cubic structure of Gd coexisted. For the hydrogenated state, a peak newly appeared at $2\theta \sim 26.6^\circ$ corresponding to hexagonal GdH₃, and a peak corresponding to cubic GdH₃ appeared at $2\theta \sim 28.9^\circ$, indicating a structural change from Gd to GdH₃ owing to hydrogenation and the coexistence of hexagonal and cubic [26] GdH₃. In the dehydrogenated state, the peak corresponding to the fluorite structure of GdH₂ appeared at $2\theta \sim 29.0^\circ$, indicating that the dehydrogenation changed the crystal structure from hexagonal and cubic GdH₃ to cubic GdH₂. Figure 2(b) shows the as-deposited state of the ad-GdH₂ (H₂: 50 %) sample, indicating that the films with the GdH₂ fluorite structure were directly synthesized. In the hydrogenated state of these films, a peak corresponding to cubic GdH₃ was appeared at $2\theta \sim 28.6^\circ$, indicating that the dehydrogenation changed the crystal structure from cubic GdH₃ to cubic GdH₂. We also confirmed that the XRD of all the ad-GdH₂ (5 %, 20 %, and 30 %) samples showed the same GdH₂ fluorite structure in the as-deposited and dehydrogenated states.

Furthermore, the XAFS spectra of the ad-Gd and ad-GdH₂ (H₂: 50 %) samples in the dehydrogenated state and the XAFS spectra of the ad-GdH₂ (H₂: 50 %) sample in the as-deposited state were almost identical, confirming that these three states possessed the same GdH₂ local structure. The extended X-ray absorption fine structure analysis was used to obtain the Gd–Gd bond distance, which was estimated to be 3.73 Å for the dehydrogenated states (ad-Gd and ad-GdH₂ (H₂: 50 %) samples) and the as-deposited state (ad-GdH₂ (H₂: 50 %) sample), in agreement with the value for

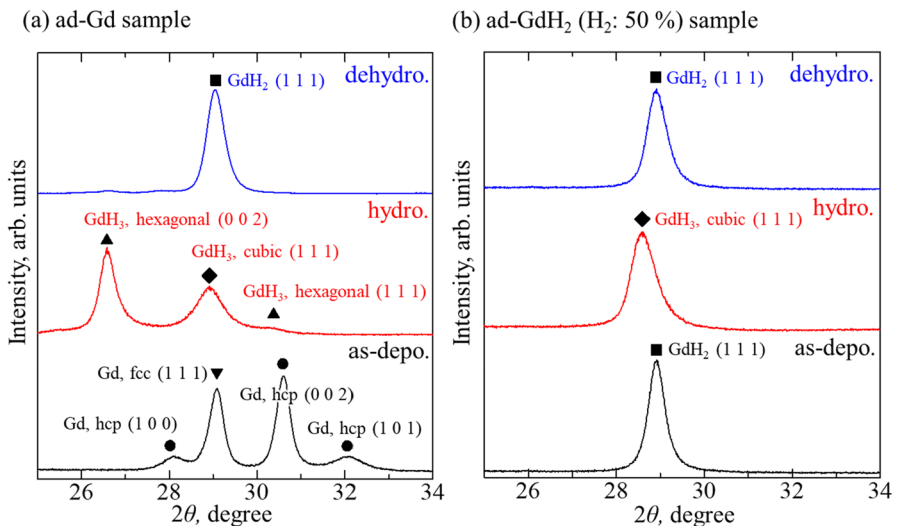


Fig. 2 XRD patterns of the Pd/Gd or Pd/GdH₂ films with the ad-Gd and ad-GdH₂ (H₂: 50 %) samples for the as-deposited, hydrogenated, and dehydrogenated states. ●: Gd in the hexagonal close-packed structure, ▼: Gd in the face-centered cubic structure, ▲: GdH₃ in the hexagonal structure, ◆: GdH₃ in the cubic structure, and ■: GdH₂ in the fluorite structure

cubic GdH_2 . Different spectra were found for the ad-Gd sample in the as-deposited state and the hydrogenated state. From the former, we obtained a Gd–Gd distance of 3.58 Å, close to the value of hexagonal metallic Gd, whereas, for the latter, it was 3.68 Å, shorter than that of GdH_2 , in agreement with previous studies [26, 27]. (See Supplementary information, Fig. S2.)

Figure 3 shows the cross-sectional bright-field and dark-field TEM images of the ad-Gd and ad- GdH_2 (H_2 : 50 %) samples. Figures 3(b) and (f) show ad-Gd sample after one cycle of hydro-/dehydrogenation, and Fig. 3(d) and (h) show ad- GdH_2 (H_2 : 50 %) sample after two cycles of hydro-/dehydrogenation. The bright-field images in Fig. 3 (a)–(d) show the results of volume expansion accompanied with the hydro-/dehydrogenation. The thickness of the film increased by 13 % from the as-deposited state (Gd) to the dehydrogenated state (GdH_2) in the ad-Gd sample, whereas in the ad- GdH_2 (H_2 : 50 %) sample, a thickness increased by 2 % was observed from the as-deposited state (GdH_2) to the dehydrogenated state (GdH_2). Despite those volume expansions, any defect and damage were not observed at the interfaces of the layers and the substrate, and the Pd layer uniformly covered the top surface. The dehydrogenated ad-Gd sample (Fig. 3(f)) exhibits a columnar-like structure, which basically reflects that of the as-deposited Gd. The ad- GdH_2 (H_2 : 50 %) sample shows more fiber-like (Fig. 3(h)) structure, which is attributed to vapor-phase crystallization upon reactive sputtering.

Figure 4 shows changes in optical transmittance upon hydro-/dehydrogenation for the bilayer ad-Gd and ad- GdH_2 (H_2 : 50 %) samples. The optical transmittance spectra of ad-Gd and ad- GdH_2 (H_2 : 50 %) samples were measured for one and two cycles of hydro-/dehydrogenation, respectively. For both samples, the film in the dehydrogenated state was opaque due to free electrons, whereas it was transparent in the visible-to-infrared range upon hydrogenation owing to the reduction of free electrons. For the ad- GdH_2 (H_2 : 50 %) sample, the transmittance spectra were reproducible for two cycles of hydro-/dehydrogenation. The changes in optical transmittance for ad- GdH_2 (H_2 : 5 %, 20 %, and 30 %) samples are shown in Fig. S3 of Supplementary information.

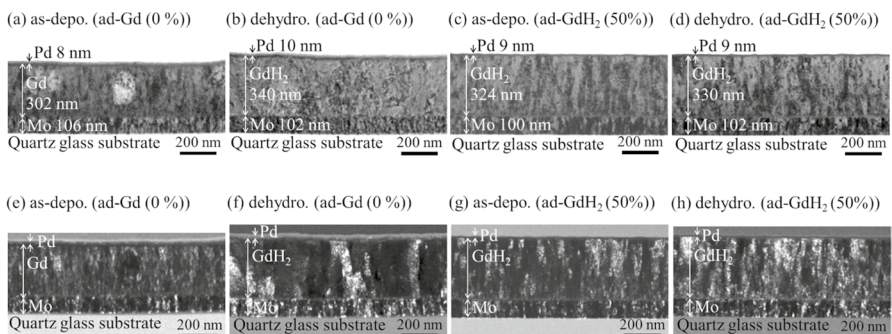


Fig. 3 (a)–(h) Cross-sectional TEM images of the Pd/Gd/Mo or Pd/GdH₂/Mo films with the ad-Gd or ad-GdH₂ (H_2 : 50 %) samples in the as-deposited and dehydrogenated states. (a)–(d) bright-field images and (e)–(h) dark-field images

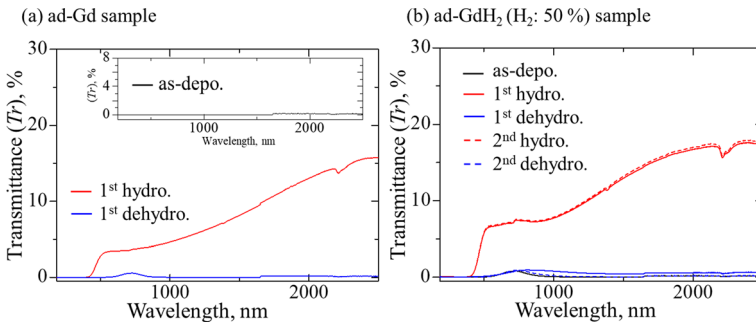


Fig. 4 Optical transmittance spectra of the Pd/Gd or Pd/GdH₂ (H₂: 50 %) samples, respectively, in the as-deposited, hydrogenated, and dehydrogenated states

3.2 Thermal and Electrical Conductivities Switchings

Figure 5 shows the thermoreflectance signals for the ad-Gd and ad-GdH₂ (H₂: 50 %) samples in the as-deposited, hydrogenated and dehydrogenated states. The thermoreflectance measurements of ad-Gd and ad-GdH₂ (H₂: 50 %) samples were conducted for one and two cycles of hydro-/dehydrogenation, respectively. The transient signal corresponded to the decrease in the temperature of the heated surface after laser heating. The thermoreflectance signals obviously changed between hydrogenation and dehydrogenation. Note that for the ad-GdH₂ sample, the signal of the as-deposited state was comparable with those of the first and second dehydrogenated states. (See Supplementary information, Fig. S4(d).) The thermoreflectance signals and cycle reproducibility for ad-GdH₂ (H₂: 5 %, 20 %, and 30 %) are shown in Figs. S4(a)–(c) and S5 of Supplementary information. Figure 6(a) shows the thermal conductivities of the ad-Gd and ad-GdH₂ (H₂: 50 %) samples in the as-deposited, hydrogenated, and dehydrogenated states. The thermal conductivities of the ad-Gd sample were 7.3 W m⁻¹ K⁻¹, 1.3 W m⁻¹ K⁻¹, and 8.3 W m⁻¹ K⁻¹ for

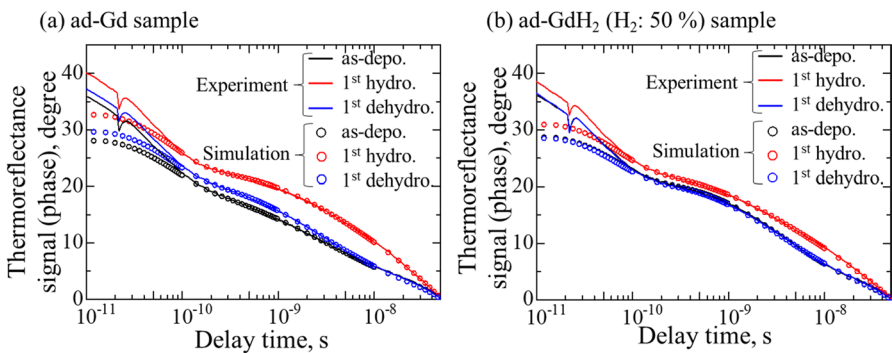


Fig. 5 Thermoreflectance signals (phase) of (a) Pd/Gd/Mo and (b) Pd/GdH₂/Mo films with the ad-Gd and ad-GdH₂ (H₂: 50 %) samples, respectively, in the as-deposited, hydrogenated, and dehydrogenated states

the as-deposited, hydrogenated, and dehydrogenated states, respectively. The relative uncertainties of the thermal conductivities, which is calculated from geometric mean of relative uncertainties of volumetric heat capacity and thermal diffusivity, for all states were $\sim 12\%$. (See Supplementary Information, Figs. S6 and S7.) The average thermal conductivities of the first and second hydrogenated states of the ad-GdH₂ (H₂: 5 %, 20 %, 30 %, and 50 %) samples were $1.6 \text{ W m}^{-1} \text{ K}^{-1}$, $1.9 \text{ W m}^{-1} \text{ K}^{-1}$, $1.4 \text{ W m}^{-1} \text{ K}^{-1}$, and $1.8 \text{ W m}^{-1} \text{ K}^{-1}$, respectively. The average thermal conductivities of the first and second dehydrogenated states of the ad-GdH₂ (H₂: 5 %, 20 %, 30 %, and 50 %) samples were $8.7 \text{ W m}^{-1} \text{ K}^{-1}$, $5.6 \text{ W m}^{-1} \text{ K}^{-1}$, $5.4 \text{ W m}^{-1} \text{ K}^{-1}$, and $6.9 \text{ W m}^{-1} \text{ K}^{-1}$, respectively. The relative uncertainties of the thermal conductivities of the ad-GdH₂ (H₂: 5 %, 20 %, 30 %, and 50 %) samples for all states were $\sim 8.7\%$. (See Supplementary information, Fig. S7–S15.) The thermal switching ratios (TSR) of the ad-Gd and ad-GdH₂ (H₂: 5 %, 20 %, 30 %, and 50 %) samples, which is the ratio of the thermal conductivity of the ON state to that of the OFF state, were 6.4, 5.4, 2.9, 3.9, and 3.9, respectively. Figure 6(b) shows the electrical conductivities of the ad-Gd and ad-GdH₂ (H₂: 50 %) samples in the as-deposited, hydrogenated, and dehydrogenated states. The electrical conductivity changes upon hydro-/dehydrogenation showed the same trend as the thermal conductivity changes. For the ad-GdH₂ (H₂: 5 %, 20 %, 30 %, and 50 %) samples, 2-cycle reproducibilities were confirmed for both thermal and electrical conductivities. (See Supplementary information, Fig. S16.) Fig. 7 shows the relationship between thermal and electrical conductivities, in which the straight line indicates the WFL at 298.15 K with a Lorentz number of $2.45 \times 10^{-8} \text{ W } \Omega \text{ K}^{-2}$. In all the ad-Gd and ad-GdH₂ samples, a series of thermal conductivity changes for Gd, GdH₃, and GdH₂ had a slope similar to that of the WFL estimation. The electrical and thermal conductivities of the dehydrogenated GdH₂ states of the GdH₂ (H₂: 20 %, 30 %, and 50 %) are smaller than those of GdH₂ (H₂: 0 % and 5 %), which could be explained in terms of the excess incorporation of hydrogens in the fluorite GdH₂ structure.

Figure 8 shows comparison of the TSR near RT for our samples to that of other thermal switching materials [1, 3, 4, 6, 10, 11]. The compared materials here

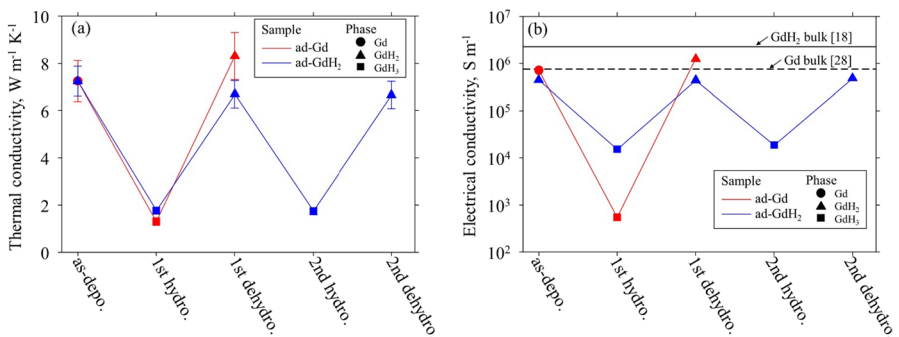
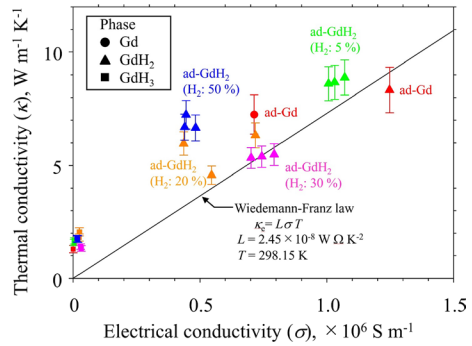


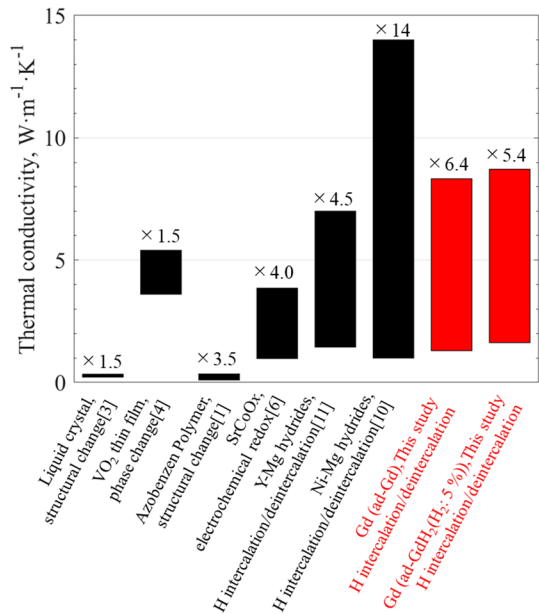
Fig. 6 (a) Thermal conductivities of the ad-Gd and ad-GdH₂ (H₂: 50 %) samples in the as-deposited, hydrogenated, and dehydrogenated states. (b) Electrical conductivities with the ad-Gd and ad-GdH₂ (H₂: 50 %) samples in the as-deposited, hydrogenated, and dehydrogenated states. The lines are guide for eyes

Fig. 7 Thermal conductivity (κ) as a function of electrical conductivity (σ). Symbols of circle, triangle and square indicate Gd, GdH_2 , and GdH_3 , respectively



are chosen based on solid substances and dry process switching. The TSR of the azobenzene polymer was reported to be 3.5, whose thermal conductivity is controlled owing to the structural change due to UV irradiation. For the liquid crystal, a structural network was changed by the magnetic field, and its TSR reached 1.5. The TSR of the sputtered VO_2 thin film associated with metal-to-insulator transition was 1.5 and that of SrCoO_x upon electrochemical oxidation/reduction was 4.0. In this study, the second largest switching ratio of 6.4 (Gd start film) was obtained after the Ni–Mg switchable mirror thin film. The TSRs for the switchable mirror materials such as the Gd, Y–Mg, and Ni–Mg are large compared to those reported from many other dry processes. The GdH_2 start thin film could be expected for practical use as a thermal switching material because of its high TSR and small volume expansion due to hydrogenation and hence the high durability.

Fig. 8 Summary of the TSR near RT for various thermal switching materials using the dry process (The labels above each bar denote the TSR)



4 Conclusion

The Gd and Gd hydride films as the switchable mirror materials were investigated for their potential use in thermal switching devices. The in situ analyses of the structural, optical, electrical, and thermophysical properties of the films were conducted during gasochromic hydro-/dehydrogenation using diluted H_2 gas (3 %), indicating the clear control between the metallic Gd and GdH_2 and semiconductor GdH_3 states. The TSR were 6.4 and 2.9–5.4 for the ad-Gd film (the Gd film in the as-deposited state) and the ad- GdH_2 (H_2 : 5 %, 20 %, 30 %, and 50 %) films (the GdH_2 films in the as-deposited state), respectively, indicating their high potential as the thermal switching layer. The thermal conductivity changes in this system can be estimated using the Wiedemann–Franz Law (WFL) and electrical conductivities.

Supplementary Information The online version contains supplementary material available at <https://doi.org/10.1007/s10765-023-03322-y>.

Acknowledgements This work was partially supported by JSPS Grants-in-Aid for Scientific Research (KAKENHI, Grant Number 23H01362) and JST CREST (grant number JPMJCR1861). TEM analyses were conducted at the Center for Instrumental Analyses, College of Science and Engineering, Aoyama Gakuin University. XAFS measurements were conducted at the BL11S2 and BL5S1 of Aichi Synchrotron Radiation Center, Aichi Science & Technology Foundation, Aichi, Japan (proposal numbers 202302122 and 202303046).

Author Contributions Riko Hirata: Investigation, Fabrication of all the samples, All in situ analyses, Writing original draft. Yuichiro Yamashita: Analyses on thermophysical properties, Investigation, Writing & review, Validation. Takashi Yagi: Analyses on thermophysical properties, Investigation, Writing & review, Validation, Funding acquisition. Makoto Kashiwagi: Investigation, Deposition of the films. Satoshi Takeya: In situ XRD analysis, Writing & review. Yuki Oguchi: TEM analysis, Visualization of TEM images. Fabio Iesari: XAFS, Writing & review. Toshihiro Okajima: XAFS, Writing & review. Naoyuki Taketoshi: Analyses on thermophysical properties, Writing & review, Validation. Yuzo Shigesato: Proposal of research content, Material suggestions, Investigation, Writing & review, Editing.

Funding This work was supported by JSPS Grants-in-Aid for Scientific Research (KAKENHI) (Grant number [23H01362]) and JST CREST (Grant number [JPMJCR1861]).

Data Availability Data sharing not applicable to this article as no datasets were generated or analyzed during the current study.

Declarations

Competing interests Not applicable.

Ethical Approval Not applicable.

Open Access This article is licensed under a Creative Commons Attribution 4.0 International License, which permits use, sharing, adaptation, distribution and reproduction in any medium or format, as long as you give appropriate credit to the original author(s) and the source, provide a link to the Creative Commons licence, and indicate if changes were made. The images or other third party material in this article are included in the article's Creative Commons licence, unless indicated otherwise in a credit line to the material. If material is not included in the article's Creative Commons licence and your intended use is not permitted by statutory regulation or exceeds the permitted use, you will need to obtain permission directly from the copyright holder. To view a copy of this licence, visit <http://creativecommons.org/licenses/by/4.0/>.

References

1. G. Wehmeyer, T. Yabuki, C. Monachon, J. Wu, C. Dames, *Appl. Phys. Rev.* **4**, 1–32 (2017). <https://doi.org/10.1063/1.5001072>
2. J. Shin, J. Sung, M. Kang, X. Xie, B. Lee, K.M. Lee, T.J. White, C. Leal, N.R. Sottos, P.V. Braun, D.G. Cahill, *Proc. Natl. Acad. Sci. U.S.A.* **116**, 5973–5978 (2019). <https://doi.org/10.1073/pnas.181708211>
3. J. Shin, M. Kang, T. Tsai, C. Leal, P.V. Braun, D.G. Cahill, *ACS Marco Lett.* **5**, 955 (2016). <https://doi.org/10.1021/acsmacrolett.6b00475>
4. H. Kizuka, T. Yagi, J. Jia, Y. Yamashita, S. Nakamura, N. Taketoshi, Y. Shigesato, *Jpn. J. Appl. Phys.* **54**, 053201 (2015). <https://doi.org/10.7567/JJAP.54.053201>
5. Y. Zhang, W.M. Postiglione, R. Xie, C. Zhang, H. Zhou, V. Chaturvedi, K. Heltemes, H. Zhou, T. Feng, C. Leighton, X. Wang, *Nat. Commun.* **14**, 2626 (2023). <https://doi.org/10.1038/s41467-023-38312-z>
6. Q. Yang, H.J. Cho, Z. Bian, M. Yoshimura, J. Lee, H. Jeon, J. Lin, J. Wei, B. Feng, Y. Ikuhara, H. Ohta, *Adv. Func. Mater.* **33**, 2214939 (2023). <https://doi.org/10.1002/adfm.202214939>
7. J. Cho, M.D. Losego, H.G. Zhang, H. Kim, J. Zuo, I. Petrov, D.G. Cahill, P.V. Braun, *Nat. Commun.* **5**, 4035 (2014). <https://doi.org/10.1038/ncomms5035>
8. Q. Lu, S. Huberman, H. Zhang, Q. Song, J. Wang, G. Vardar, A. Hunt, I. Waluyo, G. Chen, B. Yildiz, *Nat. Mater.* **19**, 655–662 (2020). <https://doi.org/10.1038/s41563-020-0612-0>
9. T. Oomura, Y. Yamashita, T. Yagi, M. Kashiwagi, Y. Oguchi, N. Taketoshi, Y. Shigesato, *Proc. 43rd Jpn. Symp. Thermophys. Prop.* (2022), B231 (in Japanese)
10. H. Yagi, T. Yagi, Y. Yamashita, M. Kashiwagi, J. Jia, Y. Oguchi, N. Taketoshi, Y. Shigesato, *Appl. Phys. Express* **16**, 095503 (2023). <https://doi.org/10.35848/1882-0786/acf6a8>
11. Y. Yamashita, K. Sugimoto, T. Yagi, M. Kashiwagi, S. Takeya, Y. Oguchi, N. Taketoshi, Y. Shigesato, *Appl. Phys. Lett.* **123**, 232201 (2023). <https://doi.org/10.1063/5.0173326>
12. J.N. Huiberts, R. Griessen, J.H. Rector, R.J. Wijngaarden, J.P. Dekker, D.G. de Groot, N.J. Koeman, *Nature* **380**, 231 (1996). <https://doi.org/10.1038/380231a0>
13. K. Yoshimura, Y. Yamada, M. Okada, *Appl. Phys. Lett.* **81**, 4709 (2002). <https://doi.org/10.1063/1.1530378>
14. K. Yoshimura, S. Bao, Y. Yamada, M. Okada, *Vacuum* **80**, 684 (2006). <https://doi.org/10.1016/j.vacuum.2005.11.013>
15. Y. Yamada, M. Miura, K. Tajima, M. Okada, K. Yoshimura, *Sol. Energy Mater. Sol. Cells* **126**, 237–240 (2014). <https://doi.org/10.1016/j.solmat.2013.06.041>
16. G. Adachi, *Kidoruinokagaku* (1999), pp. 386 (in Japanese)
17. M. Wachowiak, L. Smardz, *Int. J. Hydrog. Energy* **48**, 26840–26852 (2023). <https://doi.org/10.1016/j.ijhydene.2023.03.282>
18. J.P. Burger, J.N. Daou, P. Vajda, *J. Less-Common Met.* **103**, 381–388 (1984). [https://doi.org/10.1016/0022-5088\(84\)90262-5](https://doi.org/10.1016/0022-5088(84)90262-5)
19. C.Y. Ho, R.W. Powell, P.E. Liley, *J. Phys. Chem. Ref. Data* **3**, 1 (1974). <https://doi.org/10.1063/1.3253100>
20. S. Yamanaka, K. Yamada, K. Kurosaki, M. Uno, K. Takeda, H. Anada, T. Matsuda, S. Kobayashi, *J. Alloys Compd.* **330–332**, 99–104 (2002). [https://doi.org/10.1016/S0925-8388\(01\)01448-7](https://doi.org/10.1016/S0925-8388(01)01448-7)
21. K.D. Maglic, D.Z. Pavicic, *Int. J. Thermophys.* **22**, 1833–1841 (2001). <https://doi.org/10.1023/A:1013151303111>
22. M. Uno, K. Yamada, T. Maruyama, H. Muta, S. Yamanaka, *J. Alloys Compd.* **366**, 101–106 (2004). <https://doi.org/10.1016/j.jallcom.2003.07.006>
23. T. Yagi, K. Kobayashi, *Proc. 35th Jpn. Symp. Thermophys. Prop.* (2014), B102 (in Japanese)
24. K. Oikawa, *Japan Society of Thermophysical Properties, Thermophysical properties handbook* (Yokendo, 2008) (in Japanese)
25. S.Yu. Dankov, A.M. Tishin, V.K. Pecharsky, K.A. Gschneridner, *Phys. Rev. B* **57**, 3478–3490 (1998). <https://doi.org/10.1103/PhysRevB.57.3cx478>
26. E. Shalaan, K.H. Ehses, H. Schmitt, *J. Mater. Sci.* **41**, 7454–7458 (2006). <https://doi.org/10.1007/s10853-006-0798-9>
27. M. Ellner, H. Reule, E.J. Mittemeijer, *J. Alloys Compd.* **309**, 127–131 (2000). [https://doi.org/10.1016/S0925-8388\(00\)01055-0](https://doi.org/10.1016/S0925-8388(00)01055-0)
28. R.V. Colvin, S. Legvold, F.H. Spedding, *Phys. Rev.* **120**, 741–745 (1960). <https://doi.org/10.1103/PhysRev.120.741>

Publisher's Note Springer Nature remains neutral with regard to jurisdictional claims in published maps and institutional affiliations.

Authors and Affiliations

Riko Hirata¹ · Yuichiro Yamashita^{1,2} · Takashi Yagi^{1,2} · Makoto Kashiwagi¹ · Satoshi Takeya² · Yuki Oguchi³ · Fabio Iesari⁴ · Toshihiro Okajima^{1,4} · Naoyuki Taketoshi^{1,2} · Yuzo Shigesato¹

✉ Yuichiro Yamashita
yuichiro-yamashita@aist.go.jp

✉ Yuzo Shigesato
yuzo@chem.aoyama.ac.jp

- ¹ Graduate School of Science & Engineering, Aoyama Gakuin University, Sagamihara 252-5258, Japan
- ² National Metrology Institute of Japan (NMIJ), National Institute of Advanced Industrial Science and Technology (AIST), Central 5, 1-1-1 Higashi, Tsukuba, Ibaraki 305-8565, Japan
- ³ Center for Instrumental Analysis, College of Science and Engineering, Aoyama Gakuin University, Sagamihara 252-5258, Japan
- ⁴ Aichi Synchrotron Radiation Center, 250-3 Minamiyamaguchi-Cho, Seto, Aichi 489-0965, Japan